Supporting Information

Unraveling the role of surface and interfacial defects for hydrogen production to construct an all-in-one broken-gap photocatalyst

Jingwei Li,[1,2,3] Xuyu Wang,[,4] Hongli Fang,[1] Xiaomin Guo,[1] Rongfu Zhou,[5] Cong Wang,[2] Jian Li,[2] Mohamed Nawfal Ghazzal,*[,2] Zebao Rui*[,1]*

[1] School of Chemical Engineering and Technology, The Key Laboratory of Low-carbon Chemistry & Energy Conservation of Guangdong Province, Guangdong Engineering Technology Research Center for Platform Chemicals from Marine Biomass and Their Functionalization, Sun Yat-sen University, Zhuhai 519082, China

E-mail: ruizebao@mail.sysu.edu.cn

[2] Université Paris-Saclay, UMR 8000 CNRS, Institut de Chimie Physique, Orsay, 91405 France

E-mail: mohamed-nawfal.ghazzal@universite-paris-sacalay.fr

[3] School of Chemistry and Chemical Engineering/Institute of Clean Energy and Materials/Guangzhou Key Laboratory for Clean Energy and Materials/Huangpu Hydrogen Innovation Center, Guangzhou University, Guangzhou Higher Education Mega Center No. 230 Wai Huan Xi Road, Guangzhou, 510006, P. R. China

[4] School of Environmental and Chemical Engineering, Jiangsu University of Science and Technology, Zhenjiang, China; Huizhou Research Institute of Sun Yat-sen University, Huizhou 516081, Guangdong, China

E-Mail: wangxy@just.edu.cn

[5] School of Environmental and Chemical Engineering, Foshan University, Foshan 528225, P. R. China

1. Supplementary Methods

Reagent: $Zn(CH_3COO)_2 \cdot 2H_2O$ and $FeCl_3 \cdot 6H_2O$ were purchased from Sinopharm Chemical Reagent Co. LTD. WCl_6 was purchased from Tianjin Xiensi Biochemical Technology Co. LTD. CH_3COONa and Ethylene glycol were bought from Aladdin and Macklin, respectively. All the reagents were A.R. level and directly used without further treatment.

Synthesis of $WO_{3-x}/ZnFe_2O_{4-x}$/NGWS: The NGW: $Yb^{3+}/Er^{3+}@SiO_2$ (NGWS) was first prepared via a reported method.[24] Then, the $WO_{3-x}/ZnFe_2O_{4-x}$/NGWS were synthesized through the following processes. 0.45 mmol $Zn(CH_3COO)_2 \cdot 2H_2O$ and 0.9 mmol $FeCl_3 \cdot 6H_2O$ were dissolved into a solution composed of 10 mL deionized water and 50 mL ethylene glycol. 0.15 g of NGWS was added to the above solution. After stirring for 30 min, 5 mL of 0.95 mol L^{-1} CH_3COONa solution was dropped and stirred for another 15 min. The obtained mixture was transferred to a Teflon-lined autoclave and heated at 180 °C for 12 h. The $ZnFe_2O_{4-x}$/NGWS product was obtained after natural cooling. Secondly, the obtained $ZnFe_2O_{4-x}$/NGWS powders were ultrasonically dispersed in 15 mL absolute alcohol and then added into 40 mL of 7.5 mmol L^{-1} WCl_6 absolute alcohol solution. After vibrating for 30 min, the mixture was transferred into a Teflon-lined autoclave and heated at 160 °C for 12 h. After naturally cooling to room temperature, the $WO_{3-x}/ZnFe_2O_{4-x}$/NGWS was obtained. All powder products were washed with deionized water and absolute alcohol in the centrifugal washing process and dried at 80 °C overnight.

Synthesis of $WO_{3-x}/ZnFe_2O_{4-x}$-4/NGWS: The preparation process of $WO_{3-x}/ZnFe_2O_{4-x}$-4/NGWS is the same as $WO_{3-x}/ZnFe_2O_{4-x}$/NGWS, except for the hydrothermal reaction time of $ZnFe_2O_{4-x}$/NGWS and WCl_6 anhydrous ethanol is reduced to four hours.

Synthesis of $ZnFe_2O_{4-x}$: The preparation process of $ZnFe_2O_{4-x}$ is the same as $ZnFe_2O_{4-x}$/NGWS except without adding NGWS.

Synthesis of $WO_{3-x}/ZnFe_2O_{4-x}$-C/NGWS: The $WO_{3-x}/ZnFe_2O_{4-x}$-C/NGWS was synthesized by calculating the $WO_{3-x}/ZnFe_2O_{4-x}$/NGWS at 300 °C for two hours in the air atmosphere.

Synthesis of $WO_{3-x}/ZnFe_2O_{4-x}$ and WO_{3-x}: 0.2 g of $ZnFe_2O_{4-x}$ powders were ultrasonically dispersed in 15 mL absolute alcohol. Meanwhile, 0.67 g of WCl_6 was dissolved in 40 mL of absolute alcohol solution under stirring. The above solutions were mixed uniformly in a Teflon-lined autoclave with strongly vibrated for 30 min. Then, the Teflon-lined autoclave was heated at 160 ^oC for 12 h. After cooling naturally, the obtained $WO_{3-x}/ZnFe_2O_{4-x}$ powders were washed with deionized water and absolute alcohol and dried at 80 ^oC. The preparation process of WO_{3-x} is the same as $WO_{3-x}/ZnFe_2O_{4-x}$ except for without adding $ZnFe_2O_{4-x}$.

Characterization: The crystal structures and nanostructures of samples were analyzed by X-ray diffraction patterns (XRD, *D8 ADVANCE*), Raman spectra (Renishaw inVia Laser Micro-Raman Spectrometer), X-ray photoelectron spectroscopy (XPS, *K-Alpha*$^+$ spectrometer), field emission scanning electron microscopy (SEM, Quanta 400F), Transmission electron microscopy (TEM, F30 model FEI Tecnai G2 F30 instrument). The Ultraviolet-visible-infrared (UV-vis-IR) diffuse reflectance spectra were tested by the UV-vis spectrophotometer (DRS, UV-3600). Mott-Schottky (M-S) spectra were obtained on the electrochemical workstation (CHI660E). Ag/AgCl electrode was used as the reference electrode and 1.0 mol L^{-1} of Na_2SO_4 (pH=7.0) was the electrolyte. All of the flat-band potential (E_{fb}) values in M-S plots were corrected with the equation :$E_{fb} = E_{Ag/AgCl} + 0.197$, where E_{fb} and $E_{Ag/AgCl}$ relate to the potentials *vs*. Normal Hydrogen Electrode (NHE) and Ag/AgCl electrode, respectively. The photoluminescence (PL) spectra and time-resolved photoluminescence (TRPL) spectra were performed on FLSP980. The ultrafast transient absorption (TA) spectroscopy was carried out on the 1 kHz Ti: Sapphire Coherent Astrella regenerative amplifier from Coherent (6 mJ/pulse, 35 fs (fwhm) at 400 nm), which was coupled by Helios transient absorption spectrometer (Ultrafast systems). Electron Spin Resonance (ESR) spectra were measured by the Bruker model A300 spectrometer at ~99 K temperature.

Theoretical calculation: The DFT calculations were performed using the Vienna ab initio simulation package (VASP) based on the projector augmented wave method. The Perdew–Burke–Ernzerhof functional in generalized gradient approximation (GGA) was used to treat the exchange and correlation energy. The structure optimization was

achieved up to a precision of 10^{-5} eV in total energy difference, and the Hellmann-Feynman forces were converged to 0.01 eV $Å^{-1}$ on each atom. The Kohn-Sham orbitals were expanded in plane waves with cut-off energy of 450 eV. The H_2O adsorption energy (E_{ads}) was calculated with the following equation:

$$E_{ads} = E_{m,\,surface} + E_{H_2O} - E_{H_2O-m,\,surface}$$

where $E_{m,\,surface}$ is the energy of the $ZnFe_2O_4$ (110) or $ZnFe_2O_{4-x}$ (110) surface, E_{H_2O} is the energy of a H_2O molecule in the vacuum, and $E_{H_2O-m,\,surface}$ is energy of the corresponding $ZnFe_2O_4$ (110) or $ZnFe_2O_{4-x}$ (110) surface after the adsorption of H_2O molecule. *m* refers to $ZnFe_2O_4$ or $ZnFe_2O_{4-x}$. The charge density differences were estimated through the formula $\Delta\rho = \rho A+B-\rho A-\rho B$, where ρX is the charge density of X.

Photocatalytic experiments: ~2.5 mg of the catalysts was ultrasonically dispersed in a mixture solution of 0.5 mL methanol and 3.5 mL deionized water in a 50 mL Pyrex bottle. The pyrex bottles were bubbled with Ar gas for 15 min to eliminate O_2. The pyrex bottles were irradiated for a certain time by a Xe lamp (Beijing Zhongjiao Jinyuan Technology Co. LTD, λ=420 nm-1100 nm, 300 mW cm^{-2}) to produce hydrogen. The contents of hydrogen were analyzed by gas chromatography coupled with a TCD detector (Fuli Analytical Instrument Co., Ltd.).

2. Supplementary Figures and Tables

The XRD patterns in Figure S1a, suggest that the $WO_{3-x}/ZnFe_2O_{4-x}$ components on NGWS are composed of monoclinic $W_{18}O_{49}$ (PDF#05-0392) and cubic $ZnFe_2O_4$ (PDF#22-1012) (Figure S1b, c). The $NaGd(WO_4)_2:Yb^{3+}/Er^{3+}@SiO_2$ (NGWS) shows the tetragonal $Na_{0.5}Gd_{0.5}WO_4$ peaks (PDF#25-0829). The diffraction peaks of $Na_{0.5}Gd_{0.5}WO_4$ were unaffected after doping with Yb^{3+} and Er^{3+}, and the diffraction peaks of SiO_2 were unobserved on NGWS due to its low contents, matching well with the referenced work.[1] The diffraction peaks of WO_{3-x} at 22.92°, 25.65°, 34.56°, 47.07°, 50.18°, 54.55°, and 56.74° were assigned to the (010), (210), (502), (020), (022), and (017) $W_{18}O_{49}$ crystal planes (PDF#05-0392). Notably, the combination of WO_{3-x} and $ZnFe_2O_{4-x}$ in heterojunction $WO_{3-x}/ZnFe_2O_{4-x}$ results in the redshift of

diffraction peak from 22.92° of WO_{3-x} to 23.22° of $WO_{3-x}/ZnFe_2O_{4-x}$ and then 23.48° of $WO_{3-x}/ZnFe_2O_{4-x}$/NGWS (Figure S1d), suggesting the (010) crystal plane of WO_{3-x} is strongly react with $ZnFe_2O_{4-x}$ at WO_{3-x}-$ZnFe_2O_{4-x}$ interfaces. Meanwhile, the redshift of the XRD diffraction peak is ascribed to the significantly smaller lattice planes of $ZnFe_2O_{4-x}$ (compared to WO_{3-x}), which results in the reduced lattice spacing in WO_{3-x}-$ZnFe_2O_{4-x}$ interface (Table S1).[2,3] The redshift of the XRD diffraction peak of $WO_{3-x}/ZnFe_2O_{4-x}$/NGWS (23.48°) compared to that of $WO_{3-x}/ZnFe_2O_{4-x}$ (23.22°), suggesting that the enhanced interaction of WO_{3-x}-$ZnFe_2O_{4-x}$ interfaces with the assistance of NGWS. The Raman peaks of WO_{3-x} located at 70-400 cm^{-1} belong to W-O-W or O-W-O bending modes, and those at 600-970 cm^{-1} are related to W-O stretching modes (Figure S2a).[4,5] The Raman peaks at 704 cm^{-1}, 813 cm^{-1}, and 965 cm^{-1} correspond to the W-O stretching modes (Figure S2a).[4] The $ZnFe_2O_{4-x}$ shows obvious characteristic Raman peaks of AB_2O_4 spinel structure at the 200-800 cm^{-1} range (Figure S2a).[6] The peak at 643.1 cm^{-1} attributes to the motions of O in tetrahedral AO_4 groups (A for Fe or Zn).[6] The $WO_{3-x}/ZnFe_2O_{4-x}$ and $WO_{3-x}/ZnFe_2O_{4-x}$/NGWS also show the characteristic Raman peaks of WO_{3-x}, $ZnFe_2O_{4-x}$, and NGWS. Notably, the Raman peaks at 643.1 cm^{-1} of $ZnFe_2O_{4-x}$ show a blueshift to 638.2 cm^{-1} and then to 635.8 cm^{-1} of $WO_{3-x}/ZnFe_2O_{4-x}$/NGWS, while the peak at 965.4 cm^{-1} of WO_{3-x} shows a redshift to 972.9 cm^{-1} and then to 995.6 cm^{-1} of $WO_{3-x}/ZnFe_2O_{4-x}$/NGWS, indicating a strong interaction on WO_{3-x}-$ZnFe_2O_{4-x}$ interfaces (Figures S2b, c). These shifts of Raman peaks suggest that the interaction of WO_{3-x} and $ZnFe_2O_{4-x}$ at interfaces WO_{3-x}-$ZnFe_2O_{4-x}$ mainly relates to the interaction between the W-O bond of WO_{3-x} and the A-O bond in AO_4 of $ZnFe_2O_{4-x}$ (A for Fe or Zn).

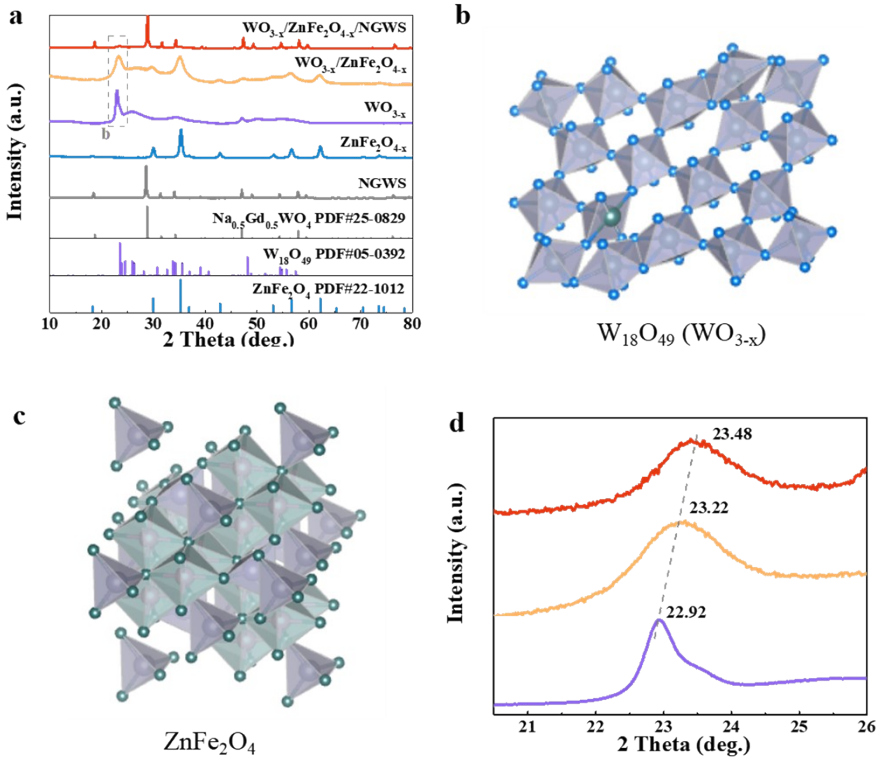

Figure S1. (a) XRD patterns of materials. Crystal structure diagrams of monoclinic (b) $W_{18}O_{49}$ (WO_{3-x}) and cubic (c) $ZnFe_2O_4$. (d) The enlarged region from (a).

Table S1. Comparison of crystal planes of $W_{18}O_{49}$ (WO_{3-x}) and $ZnFe_2O_4$.

Crystal planes of monoclinic $W_{18}O_{49}$ (Å)	Crystal planes of cubic $ZnFe_2O_4$ (Å)
$d_{(010)}$ = 3.780	$d_{(111)}$ = 4.873
$d_{(103)}$ = 3.730	$d_{(220)}$ = 2.984
$d_{(-111)}$ = 3.630	$d_{(311)}$ = 2.543
$d_{(210)}$ = 3.440	$d_{(222)}$ = 2.436
$d_{(-104)}$ = 3.390	$d_{(400)}$ = 2.109
$d_{(211)}$ = 3.170	$d_{(422)}$ = 1.723
$d_{(113)}$ = 2.654	$d_{(511)}$ = 1.624
$d_{(020)}$= 1.888	$d_{(440)}$ = 1.491

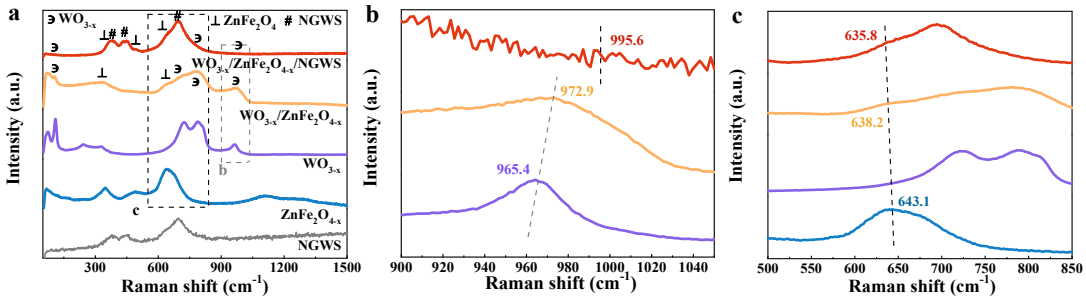

Figure S2. (a) Raman shift of the materials. (b, c) The enlarged region noted in (a).

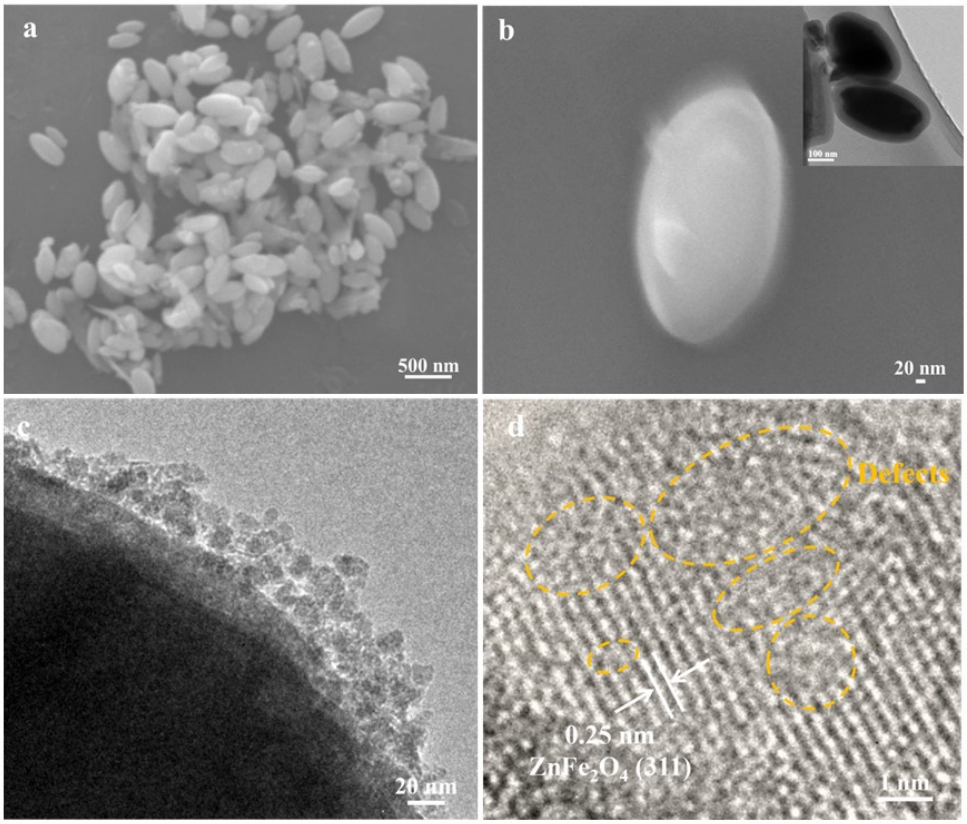

Figure S3. (a, b) SEM images of NGWS in different magnifications. TEM image of NGWS inset in (b). (c) TEM and (d) HRTEM images of $ZnFe_2O_{4-x}$/NGWS.

The SEM and TEM images in Figures S3a, b demonstrate the ellipsoid shape of NGW, which is covered by a thin layer of SiO_2 to format a core-shell nanostructure, matching well with the referenced work.[1]

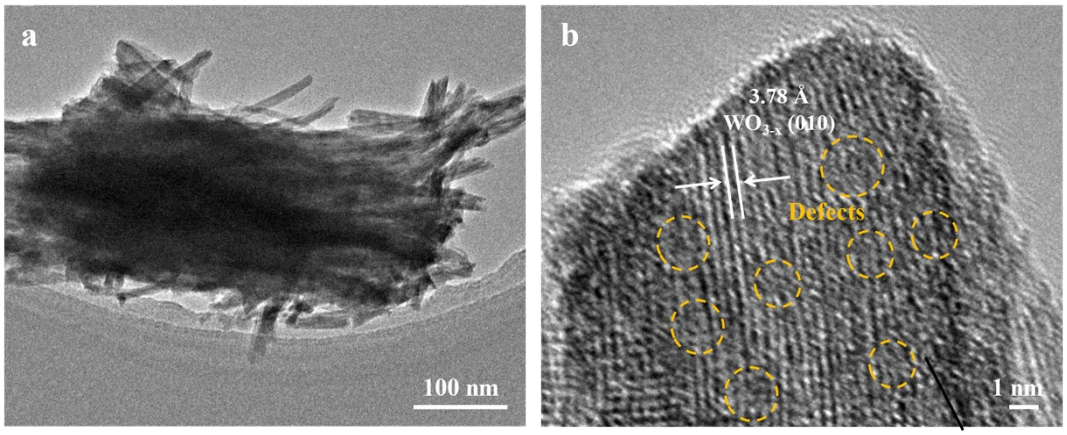

Figure S4. (a) TEM and (b) HRTEM images of WO_{3-x}.

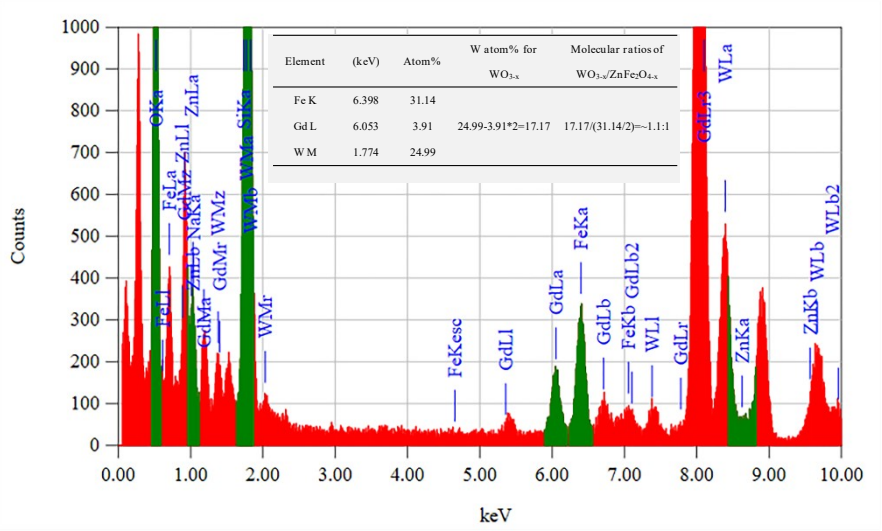

Figure S5. EDS spectrum of $WO_{3-x}/ZnFe_2O_{4-x}$/NGWS corresponds to the mapping images in Figure 1b and the corresponding specifically elemental ratios of WO_{3-x} and $ZnFe_2O_{4-x}$ of the inset table.

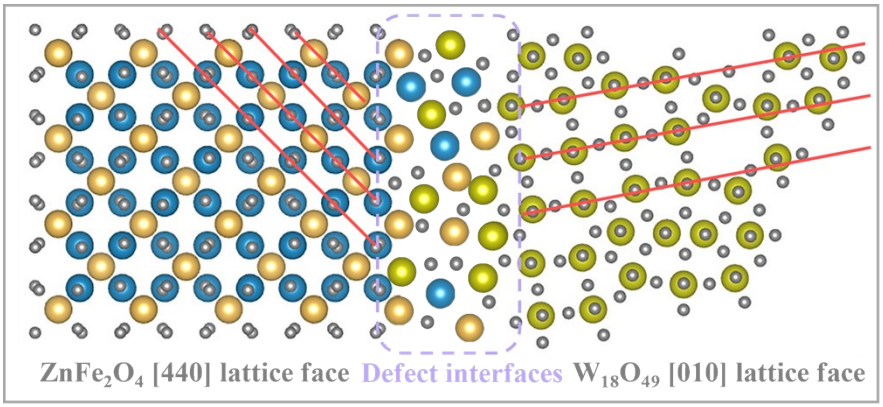

Figure S6. The schematic diagram for constructing defect WO_{3-x}-$ZnFe_2O_{4-x}$ interface.

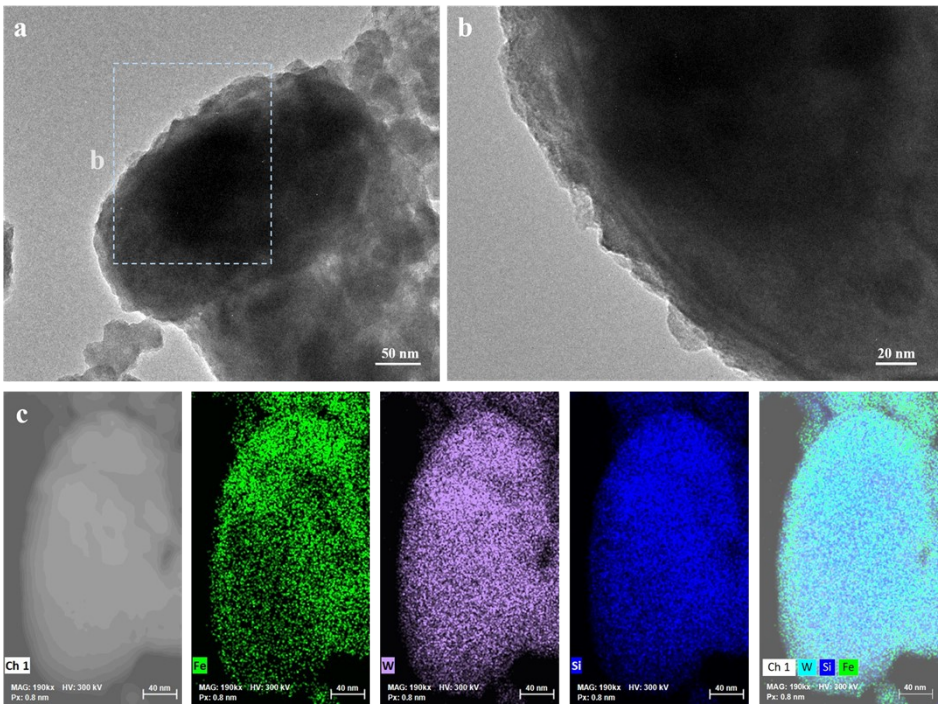

Figure S7. (a, b) TEM images and (c) elemental mapping images of $WO_{3-x}/ZnFe_2O_{4-x}$-4/NGWS.

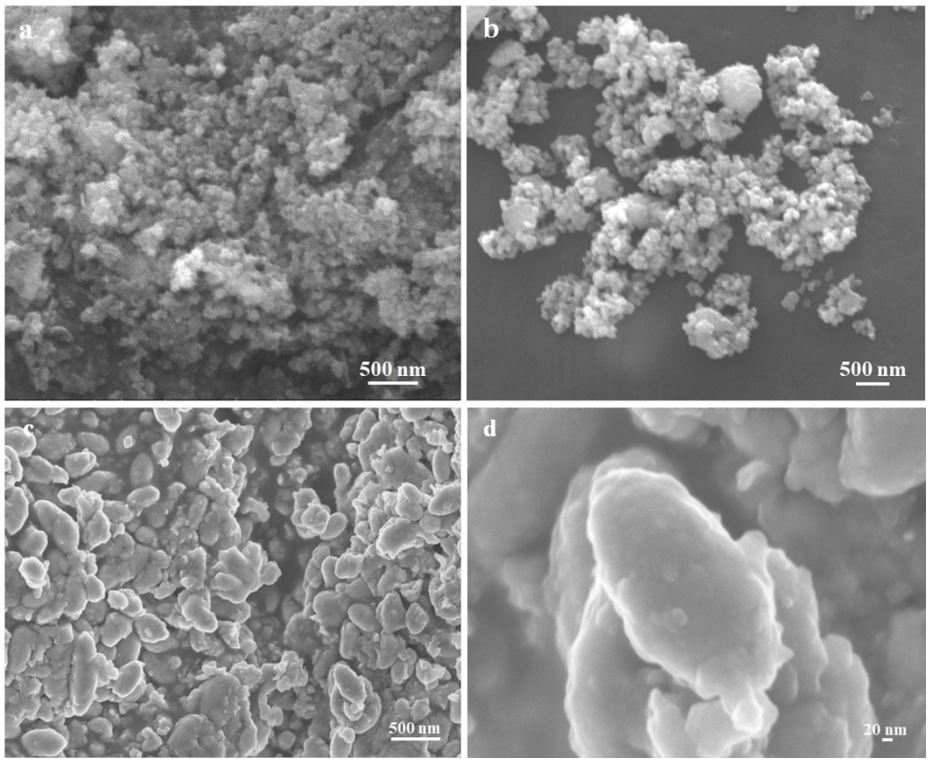

Figure S8. SEM images of (a) $ZnFeO_{4-x}$ and (b) $WO_{3-x}/ZnFe_2O_{4-x}$. (c, d) SEM images of $WO_{3-x}/ZnFe_2O_{4-x}$/NGWS with different magnifications.

The SEM image in Figure S8a shows the nanoparticles architecture of $ZnFe_2O_{4-x}$. The direct combination of WO_{3-x} and $ZnFe_2O_{4-x}$ nanoparticles without the assistance of NGWS substrate results in irregular and aggregate nanoparticles of $WO_{3-x}/ZnFe_2O_{4-x}$ with sizes of 200 nm-800 nm (Figure S8b). After growing on NGWS, the $WO_{3-x}/ZnFe_2O_{4-x}$ nanoparticles are widely dispersed (Figures S8c, d).

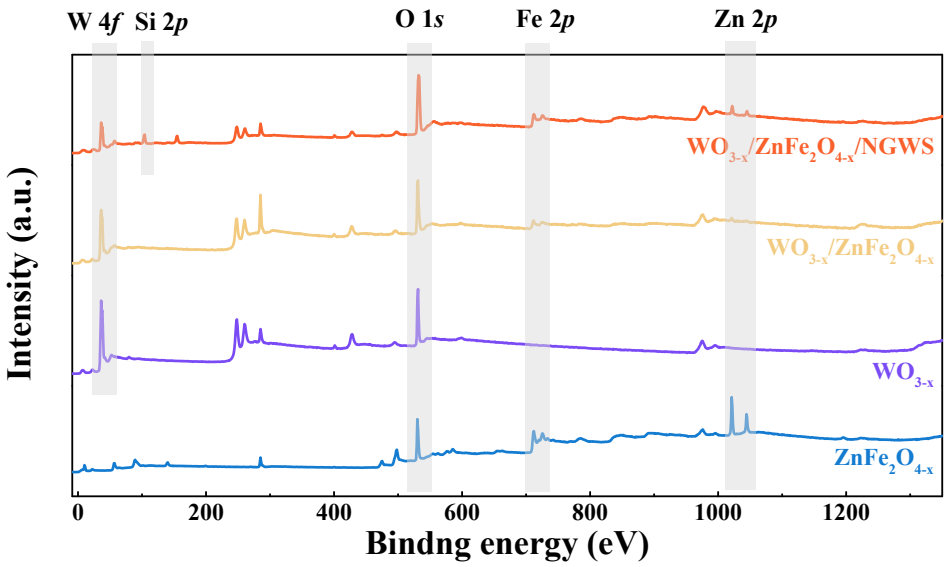

Figure S9. XPS survey spectra of samples.

The presented W 4f, O 1s, Fe 2p, and Zn 2p peaks at XPS survey spectra of heterojunctions are matched well with those at semiconductors without other impurities further verifying the successful synthesis of $WO_{3-x}/ZnFe_2O_{4-x}$/NGWS and $WO_{3-x}/ZnFe_2O_{4-x}$ heterojunction (Figure S9). The peak of Si 2p on survey spectra of $WO_{3-x}/ZnFe_2O_{4-x}$/NGWS is related to SiO_2 at surfaces of NGW.

Table S2 The calculatedly relative ratios of typical species obtained from XPS spectra of samples in Fig. 2b-d

Materials	**Fe^{2+} *vs.* all Fe species**	**W^{4+} *vs.* all W species**	**O_l *vs.* all O species**	**O_v *vs.* all O species**	**O_a *vs.* all O species**	**$O_v + O_a$ *vs.* all O species**
WZF/NGWS	0.053	0	0.24	0.28	0.48	0.76
WZF	0.043	0.020	0.65	0.26	0.09	0.35
WO_{3-x}	/	0.11	0.67	0.24	0.09	0.33
$ZnFe_2O_{4-x}$	0	/	0.85	0.10	0.05	0.15

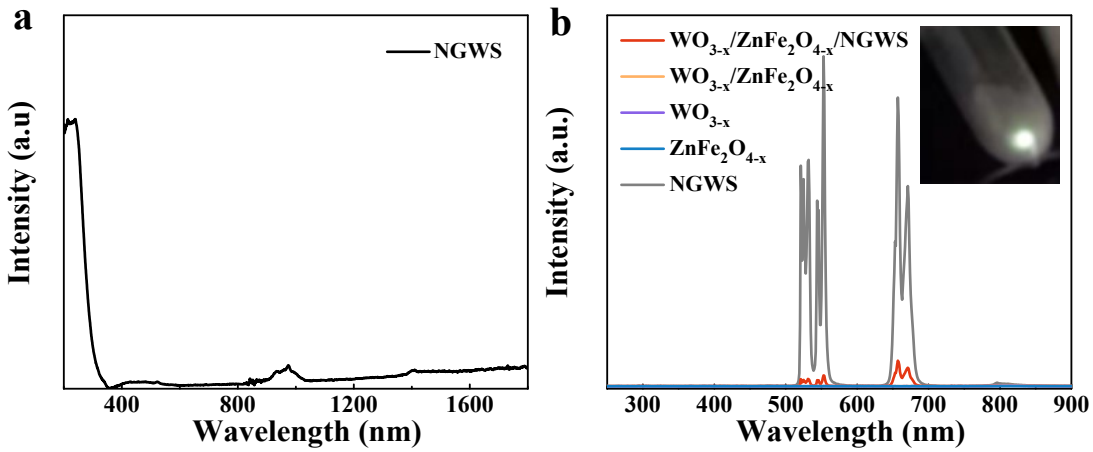

Figure S10. The UV-vis-IR spectrum of NGWS and (b) Upconversion luminescence emission spectra of materials excited with 980 nm laser (power density of 56 mW cm^{-2}). The inset photograph is the visible emission light of NGWS excited at 980 nm.

The UV-vis-IR spectrum in Figure S10a suggests the light absorption range of 200-350 nm and 900-1030 nm on NGWS. The upconversion luminescence emission spectra in Figure S10b indicate that the NGWS shows strong visible light emission at ranges of 500~590 nm and 630~720 nm under the excitation of 980 nm, while those are unsighted on $WO_{3-x}/ZnFe_2O_{4-x}$, WO_{3-x}, and $ZnFe_2O_{4-x}$. Obviously, the intensity of emission peaks of $WO_{3-x}/ZnFe_2O_{4-x}$/NGWS was significantly reduced compared to NGWS. Figure 3a indicates that the $WO_{3-x}/ZnFe_2O_{4-x}$/NGWS has strong absorption in the range of 500-720 nm. Therefore, when $WO_{3-x}/ZnFe_2O_{4-x}$ is loaded on NGWS, the visible emission energy of NGWS is absorbed by $WO_{3-x}/ZnFe_2O_{4-x}$, leading to the emission peak of $WO_{3-x}/ZnFe_2O_{4-x}$/NGWS decreases significantly in the range of 500-720 nm. Although the thin shell active components will reduce the light absorption of NGWS (UNCPs) to a certain extent, and subsequently reduce the intensity of photoluminescence. However, it has been widely verified that the thin shell active components have a weak shielding effect on the excitation light of UNCPs,[7-9] thus the absorption of photoluminescence energy by active species is the main factor that reduces the photoluminescence intensity of NGWS. As an evidence, the absorption intensity of active components $WO_{3-x}/ZnFe_2O_{4-x}$ at the range of 500-590 nm is higher

than that of 630-720 nm (Figure 3a), which leads to the upconversion luminescence peak of $WO_{3-x}/ZnFe_2O_{4-x}$/NGWS at the range of 500-590 nm is weaker than that of 630-720 nm (Figure S10b). This result further confirms that the NGWS can effectively improve the light utilization efficiency of $WO_{3-x}/ZnFe_2O_{4-x}$. Therefore, the NGWS is not only a substrate to assist the dispersion and interaction of $WO_{3-x}/ZnFe_2O_{4-x}$ but also an UNCPs material to improve the light utilization efficiency of $WO_{3-x}/ZnFe_2O_{4-x}$/NGWS.

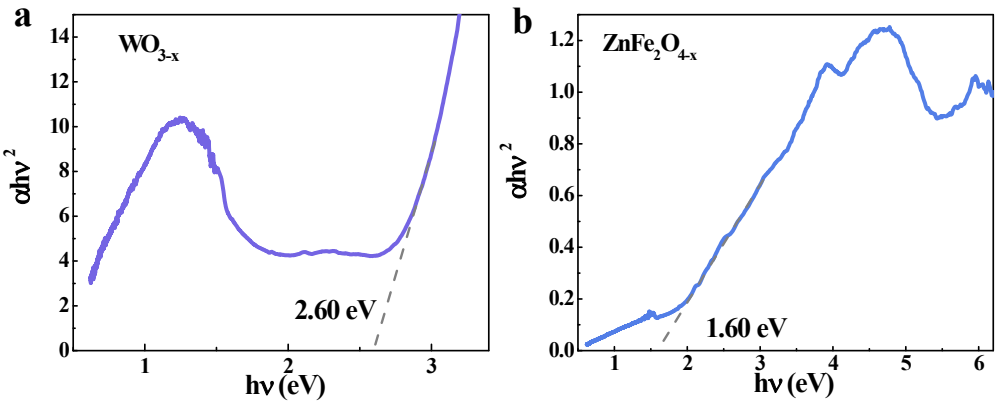

Figure S11. The plots of the square root of Kubelka-Munk function against photon energy of (a) WO_{3-x} and (b) $ZnFe_2O_{4-x}$ based on the UV-vis-IR absorption spectra in Figure 3a

Table S3 The band structure parameters of WO_{3-x} and $ZnFe_2O_{4-x}$.

Materials	Bandgaps (E_g)	Flat-band (E_{fb}) potentials	Conduction band (E_c)	Valance band (E_v)	Fermi level (E_f)
WO_{3-x}	2.6 eV	0.30 V	0.20 V	2.80 V	-0.11 V
$ZnFe_2O_{4-x}$	1.6 eV	-0.05 V	-1.55 V	0.05 V	-0.01 V

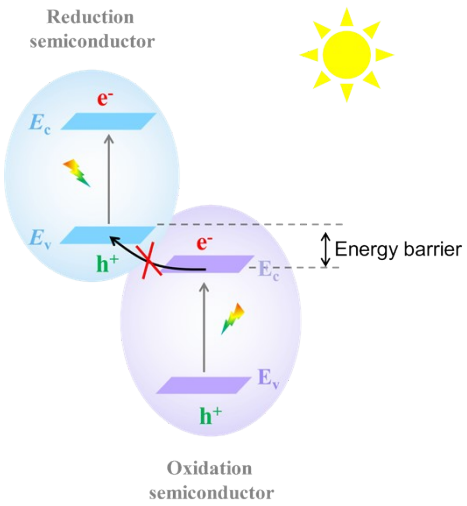

Figure S12. The summarized schematic diagram of carriers transfer in broken-gap heterojunction.

The TRPL spectra in Figure 3e were fitted with the triexponential function Equation S1 and the average decay times $\tau_{(ave)}$ were calculated according to Equation S2:[10]

$$I(t) = A_1 e^{(-t/\tau_1)} + A_2 e^{(-t/\tau_2)} + A_3 e^{(-t/\tau_3)} \quad \text{(S1)}$$

$$\tau_{ave} = \frac{A_1\tau_1^2 + A_2\tau_2^2 + A_3\tau_3^2}{A_1\tau_1 + A_2\tau_2 + A_3\tau_3} \quad \text{(S2)}$$

Where τ_1 represents the in-band recombination lifetime of electron-hole pairs, τ_2 and τ_3 relate to non-radiative lifetime in the interface, A_1, A_2, and A_3 are the corresponding amplitudes.

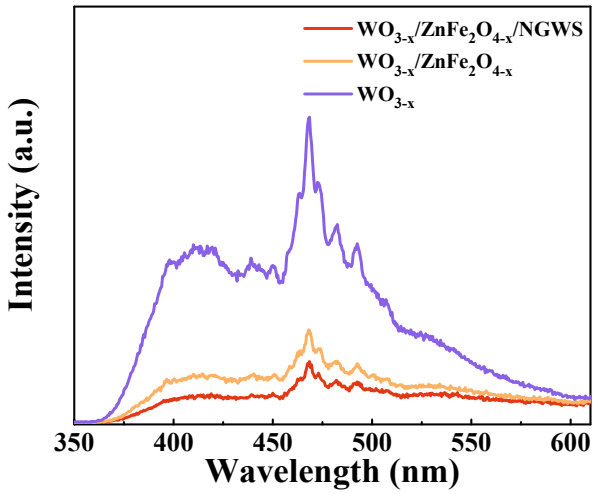

Figure S13. (a) PL spectra of samples.

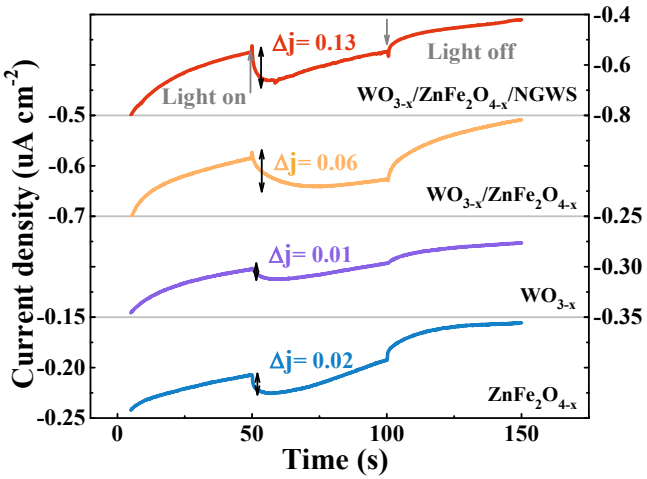

Figure S14. Photocurrent curves under the light "ON/OFF" illumination of materials.

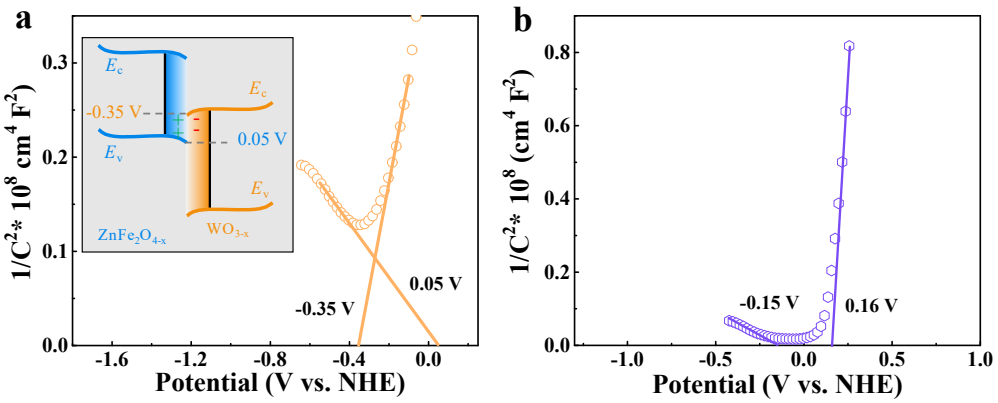

Figure S15. Mott-Schottky plots of (a) WO_{3-x}/$ZnFe_2O_{4-x}$ and (b) WO_{3-x} and $ZnFe_2O_{4-x}$ physical mixture (WO_{3-x}+$ZnFe_2O_{4-x}$). Inset in (a) is the corresponding diagrams of internal electric fields in WO_{3-x}-$ZnFe_2O_{4-x}$ interfaces with band bending.

The Mott-Schottky (M-S) plot of the WO_{3-x}+$ZnFe_2O_{4-x}$ mixture with positive and negative slopes indicates the obvious *n-p* type characteristics (Figure S15b). However, the WO_{3-x}+$ZnFe_2O_{4-x}$ mixtures show a non-overlapped *n-p* channel range (or built-in electric field), suggesting no charge transfer channel formatted in WO_{3-x}+$ZnFe_2O_{4-x}$ mixtures.

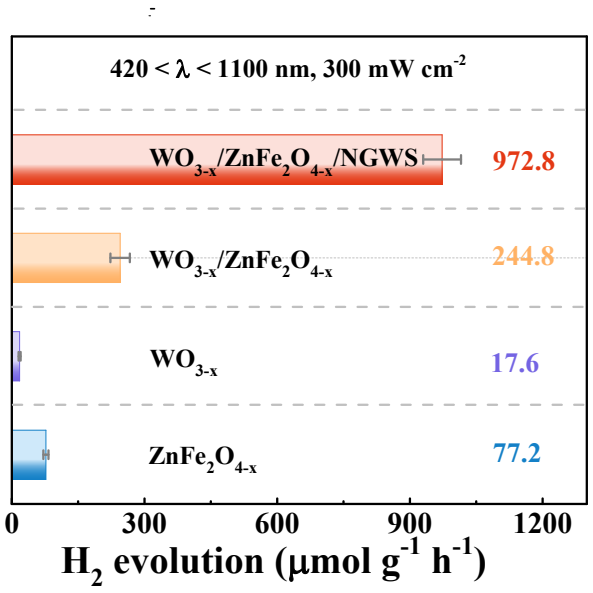

Figure S16. Photocatalytic H_2 yielding rates of materials.

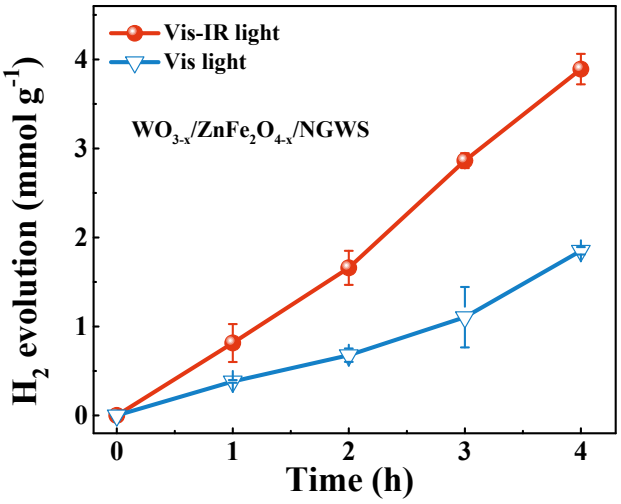

Figure S17. Photocatalytic H_2 generation *vs* time curves of $WO_{3-x}/ZnFe_2O_{4-x}$/NGWS under Vis-IR light or visible light irradiation.

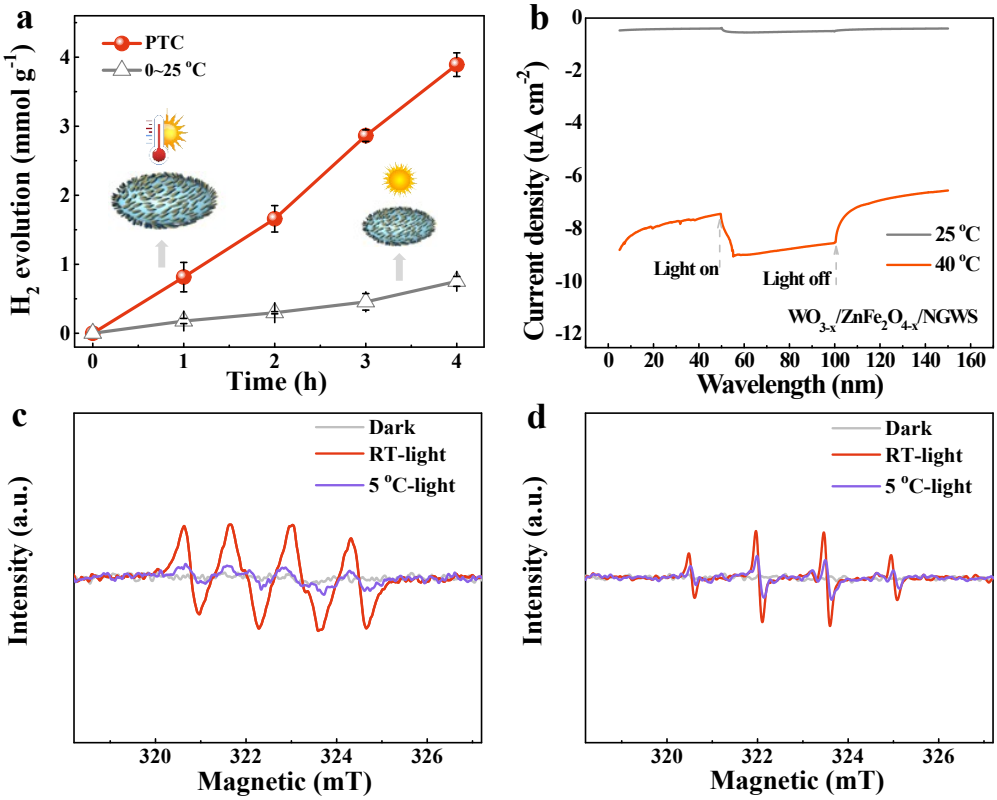

Figure S18. (a) Photocatalytic H_2 generation *vs.* time curves of $WO_{3-x}/ZnFe_2O_{4-x}$/NGWS under vis-IR light irradiation with the photoinduced thermal condition and single light irradiation with a temperature lower than 25 °C. (b) Photocurrent curves of $WO_{3-x}/ZnFe_2O_{4-x}$/NGWS at temperatures of 25 °C and 40 °C with vis-IR light irradiation. (c) DMPO-•O_2^- and (d) DMPO-•OH ESR spectra of $WO_{3-x}/ZnFe_2O_{4-x}$/NGWS at room temperature (RT) with Vis-IR light irradiation to induce photothermal effect, maintained at 5 °C with vis-IR light irradiation. The higher peak intensities of DMPO-•O_2^- and DMPO-•OH relate to higher photoredox catalytic ability.[10]

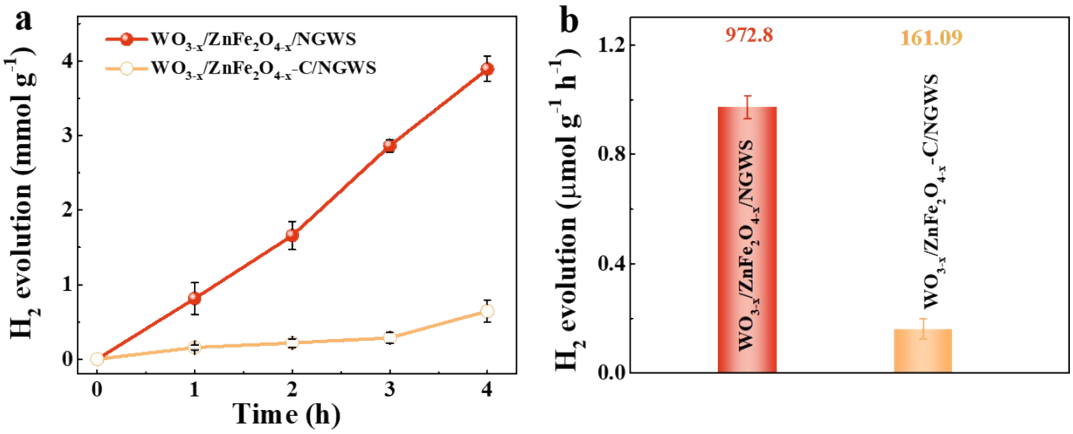

Figure S19. (a) Photocatalytic H_2 generation *vs* time curves of materials under Vis-IR light irradiation, and (b) the corresponding H_2 production rates.

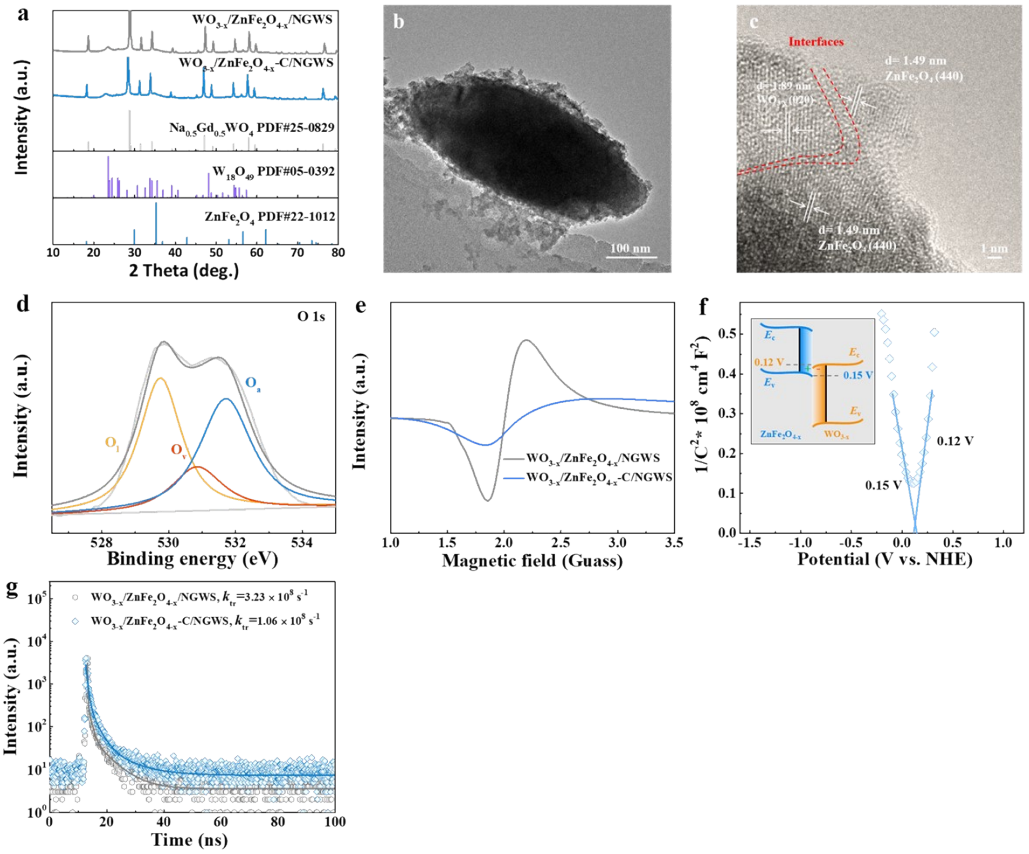

Figure S20. (a) XRD patterns. (b) TEM and (c) HRTEM images of $WO_{3-x}/ZnFe_2O_{4-x}$/NGWS after calcinating ($WO_{3-x}/ZnFe_2O_{4-x}$-C/NGWS) under air atmosphere. (d) XPS O 1*s* spectra of $WO_{3-x}/ZnFe_2O_{4-x}$-C/NGWS and $WO_{3-x}/ZnFe_2O_{4-x}$ /NGWS. (e) Powder ESR spectra. (f) Mott-Schottky (M-S) plot of $WO_{3-x}/ZnFe_2O_{4-x}$-C/NGWS. Inset in (f) is the corresponding diagrams of internal electric fields in WO_{3-x}-$ZnFe_2O_{4-x}$-C interfaces with band bending. (g) TRPL spectra.

Table S4 The calculatedly relative amount of O_v in the samples according to the fitting peak areas of O 1*s* XPS spectra in Figure S20d.

Materials	O_l *vs.* all O species	O_v *vs.* all O species	O_a *vs.* all O species	$O_v + O_a$ *vs.* all O species
$WO_{3-x}/ZnFe_2O_{4-x}$/NGWS	0.24	0.28	0.48	0.76
$WO_{3-x}/ZnFe_2O_{4-x}$-C/NGWS	0.42	0.17	0.41	0.58

The $WO_{3-x}/ZnFe_2O_{4-x}$-C/NGWS maintains crystal structure and thin film architectures of $WO_{3-x}/ZnFe_2O_{4-x}$/NGWS after calculating at 300 °C in the air

atmosphere (Figure S20a, b). However, the fitting O 1*s* spectra of $WO_{3-x}/ZnFe_2O_{4-x}$-C/NGWS (0.17) suggest that the relative amount of O_v compared to $WO_{3-x}/ZnFe_2O_{4-x}$/NGWS (0.28) is decreased although the interfacial defects were protected during the calculation (Figure S20c, d and Table S4). The fewer O_v of $WO_{3-x}/ZnFe_2O_{4-x}$-C/NGWS leads to the lower intensity of O_v ESR signal peak compared to $WO_{3-x}/ZnFe_2O_{4-x}$/NGWS (Figure S20e). The M-S plot of $WO_{3-x}/ZnFe_2O_{4-x}$-C/NGWS shows the obvious *n-p* type characteristics with positive and negative slopes (Figure S20f). Although the O_v of $WO_{3-x}/ZnFe_2O_{4-x}$-C/NGWS is reduced, its retained interfacial O_v still generates a smaller overlapped *n-p* channel region of 0.03 V (Figure S20f).

The TRPL spectra of $WO_{3-x}/ZnFe_2O_{4-x}$-C/NGWS was fitted by Equation S1 and the average decay time $\tau_{(ave)}$ was calculated according to Equation S2 to analyze the charge transfer kinetics at WO_{3-x}-$ZnFe_2O_{4-x}$-C interfaces (Figure S20g). The $WO_{3-x}/ZnFe_2O_{4-x}$-C/NGWS shows an average lifetime (τ_{ave}) of 2.91 ns. The charge tunneling rate at the WO_{3-x}-$ZnFe_2O_{4-x}$-C interface is calculated following Equation S3.[11]

$$k_{tr} = 1/\tau_{ave,WO_{3-x}/ZnFe_2O_{4-x}-C/NGWS} - 1/\tau_{ave,WO_{3-x}} \quad \text{(S3)}$$

where the $\tau_{ave,WO_{3-x}/ZnFe_2O_{4-x}-C/NGWS}$ and $\tau_{ave,WO_{3-x}}$ refer to photoexcited electrons delay average time of $WO_{3-x}/ZnFe_2O_{4-x}$-C/NGWS and WO_{3-x}, respectively. Thus, the k_{tr} of $WO_{3-x}/ZnFe_2O_{4-x}$-C/NGWS is 1.06×10^8 s^{-1}, which is lower than 3.23×10^8 s^{-1} of $WO_{3-x}/ZnFe_2O_{4-x}$/NGWS (Figure S20g).

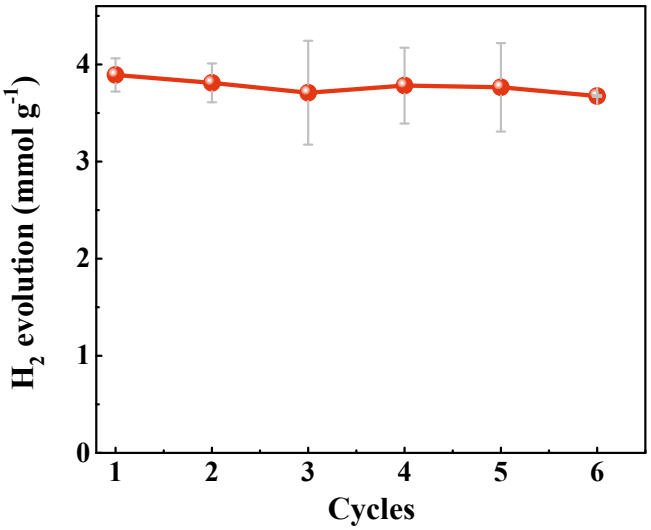

Figure S21. Recycling photocatalytic test of H_2 generation for $WO_{3-x}/ZnFe_2O_{4-x}$/NGWS (WZF/NGWS) with each cycle test under Vis-IR light irradiation for four hours.

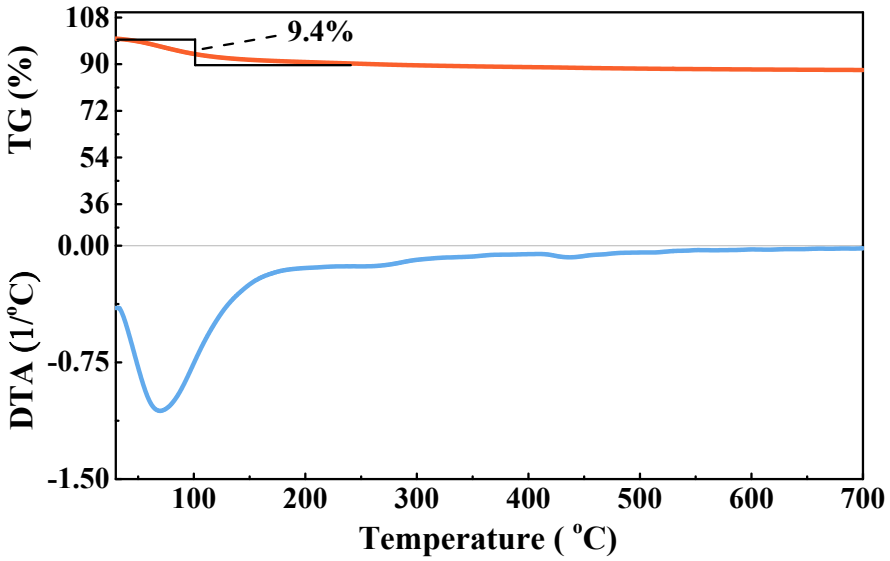

Figure S22. TG and DTA curves of $WO_{3-x}/ZnFe_2O_{4-x}$/NGWS (WZF/NGWS) tested at N_2 atmosphere.

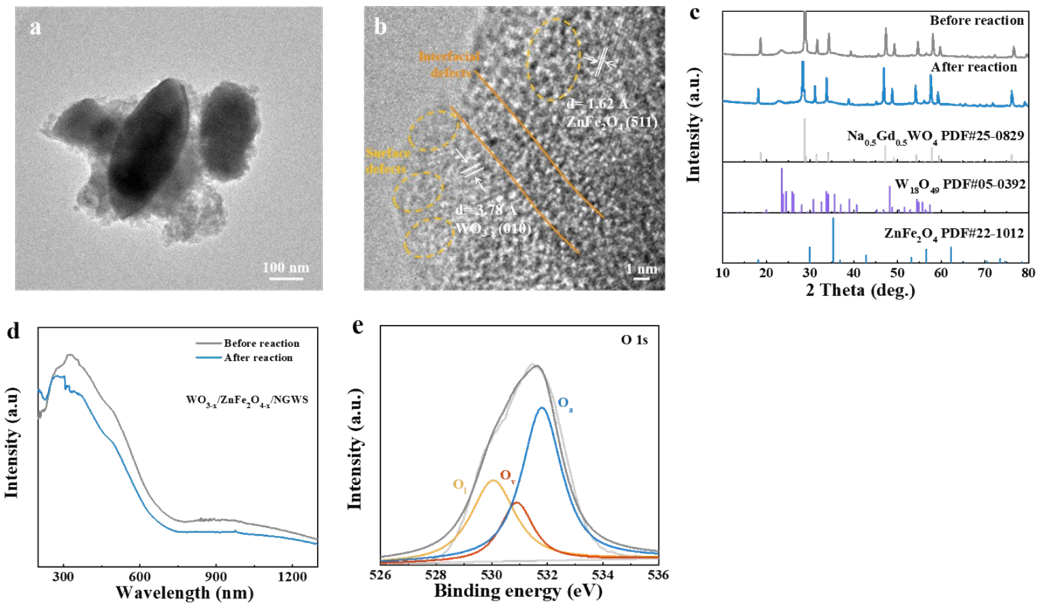

Figure S23. (a) TEM and (b) HRTEM images of $WO_{3-x}/ZnFe_2O_{4-x}$/NGWS after catalytic reaction. (c) XRD and (d) UV-vis-IR spectra of $WO_{3-x}/ZnFe_2O_{4-x}$/NGWS before and after catalytic reaction. (e) The O 1*s* XPS spectra of $WO_{3-x}/ZnFe_2O_{4-x}$/NGWS after catalytic reaction.

The O 1*s* XPS spectra of $WO_{3-x}/ZnFe_2O_{4-x}$/NGWS after catalytic reaction shown in Figure S23e just demonstrates a little decrease of the O_v+O_a value of 0.70 for oxygen vacancy defects compared to that of 0.76 before catalytic reaction (Table S2).

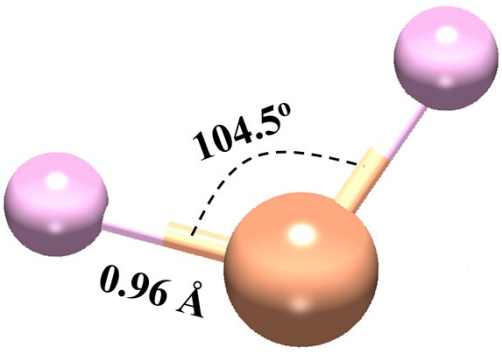

Figure S24. Crystal structure diagrams of H_2O.

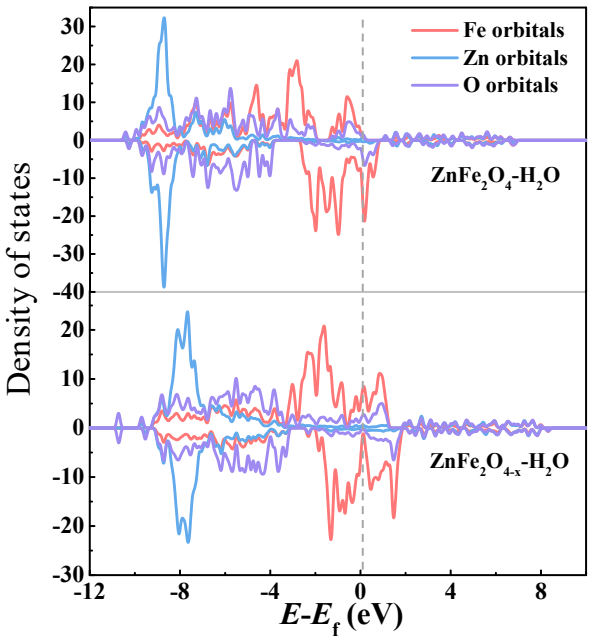

Figure S25. The calculated partial DOS of $ZnFe_2O_4$ and $ZnFeO_{4-x}$ after the absorptions of H_2O. Fermi level has been set as the reference level.

Figure S25 shows that Fe orbitals of $ZnFe_2O_4$ and $ZnFeO_{4-x}$ have higher DOS intensities near E_f level compared to Zn and O orbitals, which suggests the Fe orbitals possess a higher density of delocalized electrons and the major active sites for catalytic H_2 evolution reaction. Obviously, the regions of Fe orbitals above the E_f level of $ZnFeO_{4-x}$ are larger than those of $ZnFe_2O_4$, indicating the introduction of O_v on the surface enhances the delocalization of electrons. The delocalized electrons on surfaces favor H_2O absorption and activation.[3]

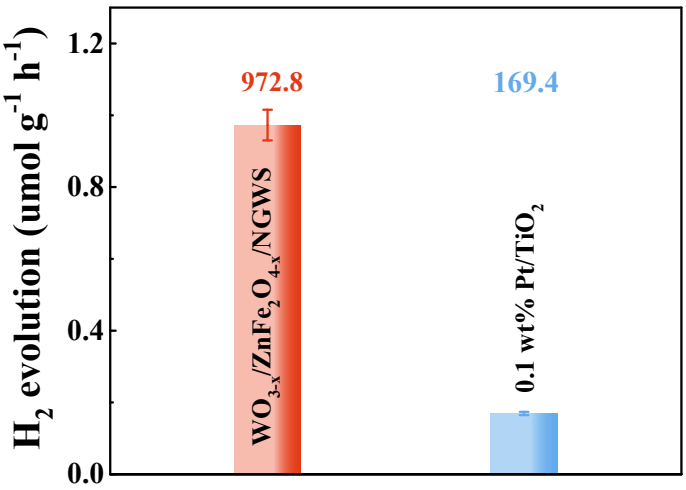

Figure S26. Photocatalytic H_2 yielding rates of $WO_{3-x}/ZnFe_2O_{4-x}$/NGWS and 0.1 wt% Pt/TiO_2 under Vis-IR light (420 nm<λ<1100 nm, 300 mW cm^{-2}) irradiation. The 0.1 wt% Pt/TiO_2 was synthesized through reduced $H_2PtCl_6 \cdot (H_2O)_6Pt$ to Pt on surfaces of TiO_2 using $NaBH_4$ as the reductant in an aqueous solution. The content of Pt on TiO_2 was determined by ICP measurement.

Table S5 The comparison of solar H_2 generation rate of $WO_{3-x}/ZnFe_2O_{4-x}$/NGWS and the recently reported materials without noble metal elements or co-catalyst.

Catalysts	Light source	Reactive solution	Photoinduced temperature (°C)	H_2 Evolution rate (μmol g^{-1} h^{-1})	Ref.
$WO_{3-x}/ZnFe_2O_{4-x}$/NGWS	300 W Xe lamp (300 mW cm^{-2}, 420 nm <λ<1100 nm)	3.5 mL water and 0.5 mL methanol	25-40	972.8	This work
$Ni_{0.17}Co_{0.83}(OH_{1-x})_2$	300 W Xe lamp (cut by 1.5 AM filter)	70 mL 1 M KOH	Maintain at 25	34.0	[S12]
[Co-1b]-COF	300 W Xe lamp (cut by 1.5 AM filter)	10 mL of acetonitrile and water in a ratio of 4:1 and 100 μL TEOA	N/A	111.0	[S13]
Co_xNi_yP-PCN	300 W Xe lamp (λ≥420 nm)	80 mL water	N/A	239.3	[S14]
3DOM $BiVO_4$	300 W Xe lamp (200 mW cm^{-2}, λ>420 nm)	0.1 M Na_2SO_3	N/A	260.0	[S15]
CN_{-x}Ni-HO	300 W Xe lamp	100 mL water and 10 mL of TEOA	N/A	354.9	[S16]
$CdSe/Zn_{1-x}Fe_xS$ QD	N/A	2.0 Ml $CdSe/Zn_{1-x}Fe_xS$ QDs solution and 0.7 mL triethylamine	N/A	393±6.7	[S17]
Ni_2P@UiO-66-NH_2	300 W Xe lamp (>380 nm)	20 mL acetonitrile, 0.2 mL deionized water and 0.6 mL triethylamine	N/A	409.1	[S18]
NH_2-MIL-125(Ti)	UV-LEDs 420 nm (32 W)	63 mL of acetonitrile, 15 mL of triethylamine and 2 mL of water	N/A	490.0	[S19]
CdS/BCNNTs	300 W Xe lamp (λ≥420 nm)	100 mL water	Maintain at 6	526.0	[S20]
PA-Ni@PCN	300 W Xe lamp (λ≥420 nm)	50 mL methanol solution (20 vol%)	N/A	713.0	[S21]
$MAPbI_3$/CoP	150 W Xe lamp (λ≥420 nm)	hydroiodic acid solution	N/A	785.9	[S22]
S-pCN/$WO_{2.72}$	300 W Xe lamp (λ>420 nm)	100 mL water and 10 mL triethanolamine	N/A	786.0	[S23]
CdS@mZnS NRs	300 W Xe lamp (λ>422 nm)	100 mL 0.25 M Na_2S, 0.35 M Na_2SO_3	Maintained at ~25	820.0	[S24]

Table S6 The comparison of solar H_2 generation rate of $WO_{3-x}/ZnFe_2O_{4-x}$/NGWS and the recently reported materials with noble metal elements or co-catalyst.

Catalysts	Light source	Types containing noble metal elements or co-catalyst	Reactive solution	Photoinduced temperature (°C)	H_2 Evolution rate (μmol g^{-1} h^{-1})	Ref.
$WO_{3-x}/ZnFe_2O_{4-x}$/NGWS	300 W Xe lamp (300 mW cm^{-2}, 420 nm <λ<1100 nm)	N/A	3.5 mL water and 0.5 mL methanol	25-40	972.8	This work
MnO_x/g-C_3N_4/CdS/Pt	300 W Xe lamp (100 mW cm^{-2})	Pt	100 mL 0.35 M Na_2S, 0.25 M Na_2SO_3	Maintained at 8	1303.4	[S25]
TJU-16-$Rh_{0.22}$	300 W Xe lamp	Rh	100 ml H_2O	Maintained at 5	31.0	[S26]
RuO_2-loaded $Ba_2Bi_3Nb_2O_{11}I$	300 W Xe (λ>400 nm)	Rh	Methanol solution (20 vol %, 100 mL)	N/A	52.0	[S27]
TiO_2–Ti_3C_2/Ru	300 W Xe lamp (350 nm <λ<780 nm)	Ru	80 mL 10% methanol solution	N/A	235.3	[S28]
PCN@HP	300 W Xe lamp (λ>400 nm)	Pt	150 mL water	Maintained at 25	350.0	[S29]
Au/TiO_2(P25)-gC_3N_4	N/A	Au	triethanolamine 1 vol%)	N/A	419.0	[S30]
PtSA/Cs_2SnI_6	300 W Xe lamp (λ≥420 nm, 100 mW cm^{-2})	Pt	Aqueous HI solution (containing 20 vol% H_3PO_2)	Maintained at 25	434.0	[S31]
$PbTiO_3$-TiO_2	300 W Xe lamp	Pt, Pb	100 mL water and 10 vol % triethanolamine	N/A	436.5	[S32]
Ultrathin g-C_3N_4 nanosheets/boron-doped g-C_3N_4 (CNN/BDCNN)	300 W Xe lamp (λ>300 nm)	N/A	90 mL water and 10 vol % triethanolamine	Maintained at 35	491	[S33]

Pt-Fc@UiO-66-NH_2	300 W Xe lamp (λ>380 nm)	Pt	0.2 mL water and 2 mL triethanolamine	N/A	514.8	[S34]
Ag-Ag_2S-CdS NPs	300 W Xe lamp (1000 mW cm^{-2}, λ>350 nm)	Ag	100 mL 0.1 M Na_2SO_3 solution	Maintained at 25	~800.0	[S35]
$Cs_3Bi_{0.6}Sb_{1.4}I_9$	N/A	Pt	aqueous HI solution	N/A	926	[S36]

References

1 L. Zheng, X. Huang, J. Zhong, Z. Wang and X. Cheng, *RSC Adv.*, 2021, **11**, 3981–3989.

2 R. Lamber, S. Wetjen and N. I. Jaeger, *Phys. Rev. B.*, 1995, **51**, 10968–10971.

3 J. Li, R. Lian, J. Wang, S. He, S. P. Jiang and Z. Rui, *Electrochim. Acta*, 2020, **331**. 135395.

4 C. Guo, S. Yin, Q. Dong and T. Sato, *RSC Adv.*, 2012, **2**, 5041.

5 C. Guo, S. Yin, M. Yan, M. Kobayashi, M. Kakihana and T. Sato, *Inorg. Chem.*, 2012, **51**, 4763–4771.

6 M. Maletin, E. G. Moshopoulou, A. G. Kontos, E. Devlin, A. Delimitis, V. T. Zaspalis, L. Nalbandian and V. V. Srdic, *J. Eur. Ceram. Soc.* 2007, **27**, 4391.

7 Y.–W. Li, L. Dong, C.–X. Huang, Y.–C. Guo, X.–Z. Yang, Y.–J. Xu and H.–S. Qian, *RSC Adv.*, 2016, **6**, 54241–54248.

8 L. Tan, D. Li, L. Zhang, L. Xu, Y. Zhao, L. Zhu and R. Qiao, *J. Phy. Chem. C*, 2020, **124**, 18081–18090.

9 S. Ullah, C. Hazra, E. P. Ferreira-Neto, T. C. Silva, U. P. Rodrigues-Filho and S. J. L. Ribeiro, *CrystEngComm*, 2017, **19**, 3465–3475.

10 J. Li, X. Yang, C. Ma, Y. Lei, Z. Cheng and Z. Rui, *Appl. Catal. B. Environ.*, 2021, **291**, 120053.

11 W. Lei, Y. Mi, R. Feng, P. Liu, S. Hu, J. Yu, X. Liu, J. A. Rodriguez, J.–O. Wang, L. Zheng, K. Tang, S. Zhu, G. Liu and M. Liu, *Nano Energy*, 2018, **50**, 552–561.

12 M. Wang, J. Q. Wang, C. Xi, C. Q. Cheng, C. Q. Zou, R. Zhang, Y. M. Xie, Z. L. Guo, C. C. Tang, C. K. Dong, Y. J. Chen and X. W. Du, *Angew. Chem. Int. Ed.*, 2020, **59**, 11510–11515.

13 K. Gottschling, G. Savasci, H. Vignolo-Gonzalez, S. Schmidt, P. Mauker, T. Banerjee, P. Rovo, C. Ochsenfeld and B. V. Lotsch, *J. Am. Chem. Soc.*, 2020, **142**, 12146–12156.

14 F. Xue, Y. Si, M. Wang, M. Liu and L. Guo, *Nano Energy*, 2019, **62**, 823–831.

15 H. Wu, R. Irani, K. Zhang, L. Jing, H. Dai, H. Y. Chung, F. F. Abdi and Y. H. Ng, *ACS Energy Lett.*, 2021, **6**, 3400–3407.

16 X. Jin, R. Wang, L. Zhang, R. Si, M. Shen, M. Wang, J. Tian and J. Shi, *Angew. Chem. Int. Ed.*, 2020, **59**, 6827–6831.

17 Y.–J. Gao, X.–B. Li, X.–Z. Wang, N.–J. Zhao, Y. Zhao, Y. Wang, Z.–K. Xin, J.–P. Zhang, T. Zhang, C.–H. Tung and L.–Z. Wu, *Matter*, 2020, **3**, 571–585.

18 K. Sun, M. Liu, J. Pei, D. Li, C. Ding, K. Wu and H. L. Jiang, *Angew. Chem. Int. Ed.*, 2020, **59**, 22749–22755.

19 X. Chen, S. Xiao, H. Wang, W. Wang, Y. Cai, G. Li, M. Qiao, J. Zhu, H. Li, D. Zhang and Y. Lu, *Angew. Chem. Int. Ed.*, 2020, **59**, 17182–17186.

20 Z. Ai, K. Zhang, D. Shi, B. Chang, Y. Shao, L. Zhang, Y. Wu and X. Hao, *Nano Energy*, 2020, **69**. 104408.

21 Y. Huang, Y. Jian, L. Li, D. Li, Z. Fang, W. Dong, Y. Lu, B. Luo, R. Chen, Y. Yang, M. Chen and W. Shi, *Angew. Chem. Int. Ed.*, 2021, **60**, 5245–5249.

22 C. Cai, Y. Teng, J. H. Wu, J. Y. Li, H. Y. Chen, J. H. Chen and D. B. Kuang, *Adv. Funct. Mater.*, 2020, **30**. 2001478.

23 X. Li, B. Kang, F. Dong, Z. Zhang, X. Luo, L. Han, J. Huang, Z. Feng, Z. Chen, J. Xu, B. Peng and Z. L. Wang, *Nano Energy*, 2021, **81**, 105671.

24 Z. Lian, M. Sakamoto, Y. Kobayashi, N. Tamai, J. Ma, T. Sakurai, S. Seki, T. Nakagawa, M. W. Lai, M. Haruta, H. Kurata and T. Teranishi, *ACS Nano*, 2019, **13**, 8356–8363.

25 J. Pan, P. Wang, P. Wang, Q. Yu, J. Wang, C. Song, Y. Zheng and C. Li, *Chem. Eng. J.*, 2021, **405**. 126622.

26 X. Song, G. Wei, J. Sun, C. Peng, J. Yin, X. Zhang, Y. Jiang and H. Fei, *Nat. Catal.*, 2020, **3**, 1027–1033.

27 K. Ogawa, H. Suzuki, C. Zhong, R. Sakamoto, O. Tomita, A. Saeki, H. Kageyama and R. Abe, *J. Am. Chem. Soc.*, 2021, **143**, 8446–8453.

28 Y. Liu, Y. H. Li, X. Li, Q. Zhang, H. Yu, X. Peng and F. Peng, *ACS Nano*, 2020, **14**, 14181–14189.

29 Y. Zhu, C. Lv, Z. Yin, J. Ren, X. Yang, C. L. Dong, H. Liu, R. Cai, Y. C. Huang, W. Theis, S. Shen and D. Yang, *Angew. Chem. Int. Ed.*, 2020, **59**, 868–873.

30 P. Jiménez–Calvo, V. Caps, M. N. Ghazzal, C. Colbeau–Justin and V. Keller, *Nano Energy*, 2020, **75**. 104888.

31 P. Zhou, H. Chen, Y. Chao, Q. Zhang, W. Zhang, F. Lv, L. Gu, Q. Zhao, N. Wang, J. Wang and S. Guo, *Nat. Commun.*, 2021, **12**, 4412.

32 G. Liu, L. Ma, L.–C. Yin, G. Wan, H. Zhu, C. Zhen, Y. Yang, Y. Liang, J. Tan and H.–M. Cheng, *Joule*, 2018, **2**, 1095–1107.

33 D. Zhao, Y. Wang, C.–L. Dong, Y.–C. Huang, J. Chen, F. Xue, S. Shen and L. Guo, *Nat. Energy*, 2021, **6**, 388–397.

34 M. Xu, D. Li, K. Sun, L. Jiao, C. Xie, C. Ding and H. L. Jiang, *Angew. Chem. Int. Ed.*, 2021, **60**, 16372–16376.

35 T. Kawawaki, T. Nakagawa, M. Sakamoto and T. Teranishi, *J. Am. Chem. Soc.*, 2019, **141**, 8402–8406.

36 G. Chen, P. Wang, Y. Wu, Q. Zhang, Q. Wu, Z. Wang, Z. Zheng, Y. Liu, Y. Dai and B. Huang, *Adv. Mater.*, 2020, **32**, 2001344.